ACS NANO

www.acsnano.org

ARTICLE

Low-Temperature and High-Quality Growth of Bi_2O_2Se Layered Semiconductors *via* Cracking Metal–Organic Chemical Vapor Deposition

Minsoo Kang,[⊡] Hyun-Jun Chai,[⊡] Han Beom Jeong, Cheolmin Park, In-young Jung, Eunpyo Park, Mert Miraç Çiçek, Injun Lee, Byeong-Soo Bae, Engin Durgun, Joon Young Kwak, Seungwoo Song,* Sung-Yool Choi,* Hu Young Jeong,* and Kibum Kang*

Cite This: *ACS Nano* 2021, 15, 8715–8723

Read Online

ACCESS | Metrics & More | Article Recommendations | Supporting Information

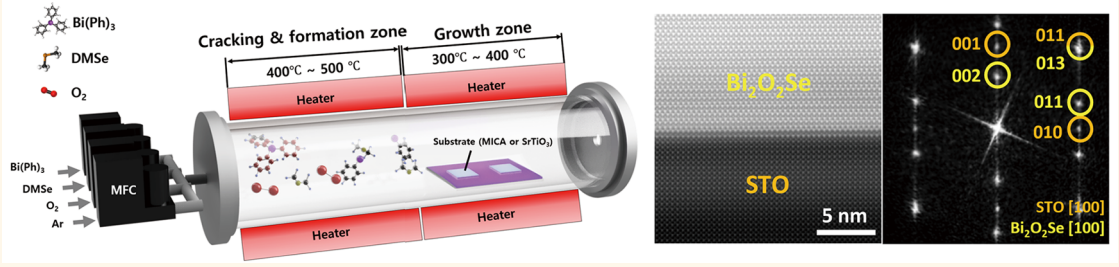

ABSTRACT: **Ternary metal-oxy-chalcogenides are emerging as next-generation layered semiconductors beyond binary metal-chalcogenides (*i.e.*, MoS_2). Among ternary metal-oxy-chalcogenides, especially Bi_2O_2Se has been demonstrated in field-effect transistors and photodetectors, exhibiting ultrahigh performance with robust air stability. The growth method for Bi_2O_2Se that has been reported so far is a powder sublimation based chemical vapor deposition. The first step for pursuing the practical application of Bi_2O_2Se as a semiconductor material is developing a gas-phase growth process. Here, we report a cracking metal–organic chemical vapor deposition (c-MOCVD) for the gas-phase growth of Bi_2O_2Se. The resulting Bi_2O_2Se films at very low growth temperature (~300 °C) show single-crystalline quality. By taking advantage of the gas-phase growth, the precise phase control was demonstrated by modulating the partial pressure of each precursor. In addition, c-MOCVD-grown Bi_2O_2Se exhibits outstanding electrical and optoelectronic performance at room temperature without passivation, including maximum electron mobility of 127 $cm^2/(V·s)$ and photoresponsivity of 45134 A/W.**

KEYWORDS: *cracking metal–organic chemical vapor deposition, bismuth-oxy-selenide, low-growth temperature, epitaxial growth, field-effect transistor, photodetector*

INTRODUCTION

Layered semiconductors (or also called van der Waals semiconductors) have received tremendous interest due to their anisotropic crystal structure with dangling bond free surface. Unlike traditional semiconductors, layered semiconductors are chemically stable even in a single-layer two-dimensional (2D) thickness[1−3] and form heterojunctions without lattice matching.[4−9] Thus, they are potentially applicable in ultrathin-body transistors[10] and multijunction optoelectronic devices.[6] The most popular layered semiconductors are binary metal-chalcogenides (*i.e.*, MoS_2), but they fail to exhibit notable advantages over the properties of traditional semiconductor materials, such as electron mobility, photoresponse, and chemical stability.[11] Accordingly, there has been a demand to seek other layered semiconductors beyond binary metal-chalcogenides.

Recently, the growth of ternary metal-oxy-chalcogenides (*i.e.*, Bi_2O_2Se) using powder sublimation was reported, and the resulting material showed high electron mobility, excellent on/off ratio, and an air-stable nature.[12,13] Furthermore, native oxide of Bi_2O_2Se (Bi_2SeO_5) can be easily obtained through

Received: January 28, 2021
Accepted: May 7, 2021
Published: May 11, 2021

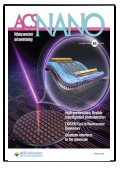

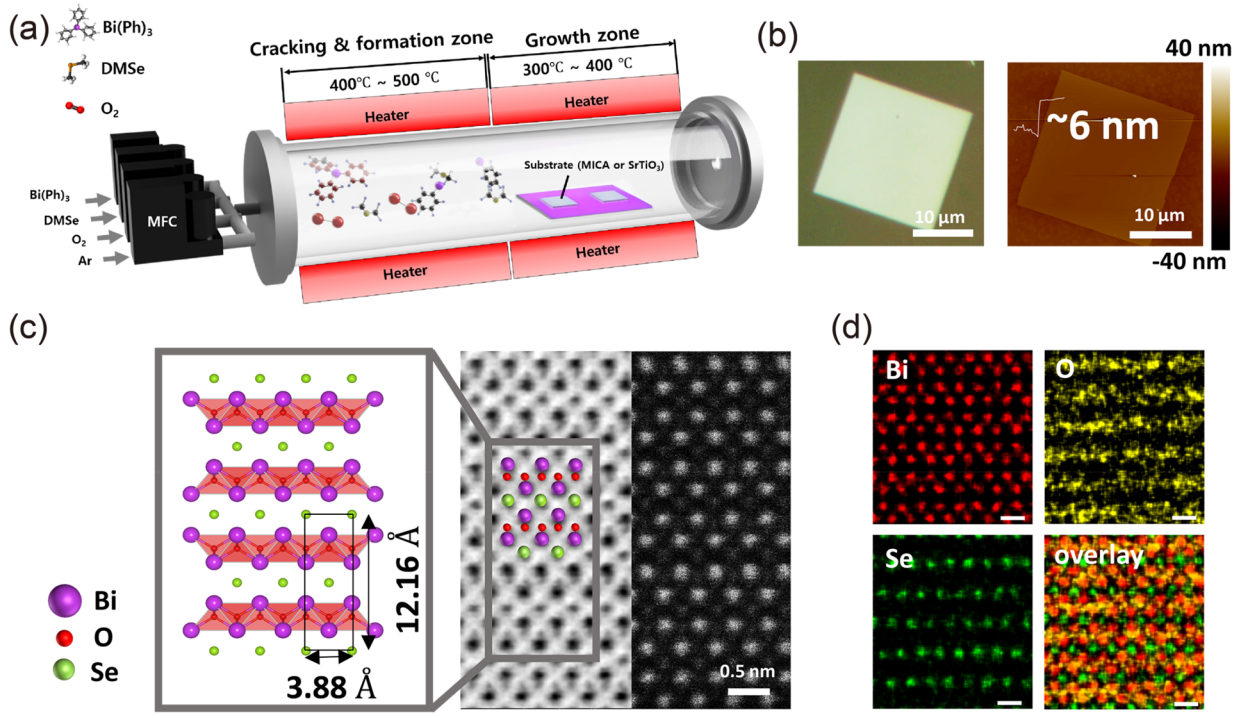

Figure 1. MOCVD Bi_2O_2Se growth. (a) Schematic illustration of two-zone c-MOCVD setup used for Bi_2O_2Se growth. (b) Typical OM and AFM images of Bi_2O_2Se nanoplate grown on mica substrate. (c) Crystal structure and atomic resolution ABF-STEM (left) and HAADF-STEM (right) images of Bi_2O_2Se viewed from the [100] direction. (d) False color Bi, O, and Se and overlaid EDS mapping of Bi_2O_2Se. Scale bar: 0.5 nm.

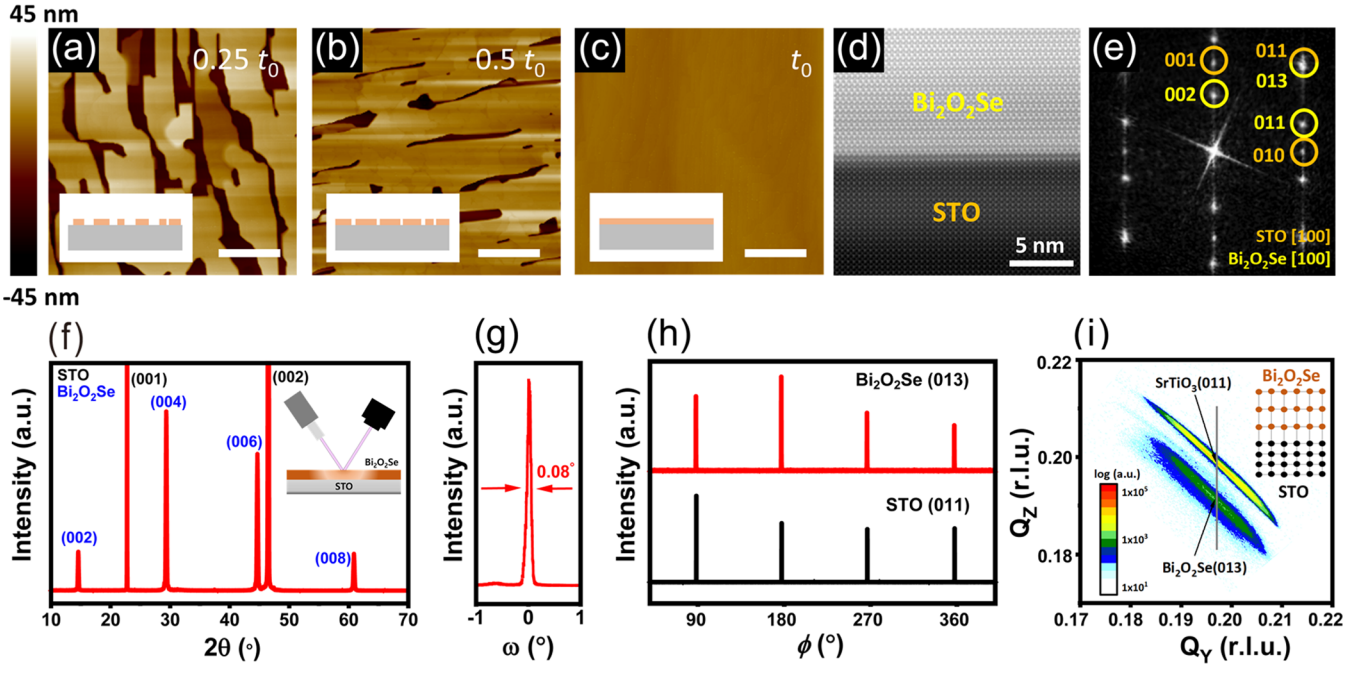

Figure 2. Single-crystalline film growth of Bi_2O_2Se on $SrTiO_3$ substrate. (a–c) AFM images of MOCVD-grown Bi_2O_2Se at different growth times, where t_0 indicates the time of the fully covered condition. Scale bar: 1 μm. (d) HAADF-STEM image of Bi_2O_2Se on STO substrate. (e) FFT pattern of the corresponding sample. (f) 2θ–ω scan in XRD measurement of Bi_2O_2Se grown on the STO substrate. (g) Rocking curve in HRXRD for (004)-plane of Bi_2O_2Se. (h) ϕ scans in HRXRD for the off-axis (013)-plane of Bi_2O_2Se and (011)-plane of STO, respectively. (i) RSM around (011)-planes of STO and (013)-planes of the Bi_2O_2Se thin film on STO substrate.

layer-by-layer thermal oxidation, which exhibits a sharp interface and low trap density due to its crystalline nature.[14,15] These fascinating properties make Bi_2O_2Se a strong candidate of channel material for next-generation transistors. In addition to field-effect transistor (FET), thanks to its small band gap (0.8–1.09 eV),[15−19] Bi_2O_2Se based photodetectors demonstrate ultrabroadband photodetecting capability from ultraviolet to infrared with high responsivity (~5800 A/W at 532

https://doi.org/10.1021/acsnano.1c00811
ACS Nano 2021, 15, 8715−8723

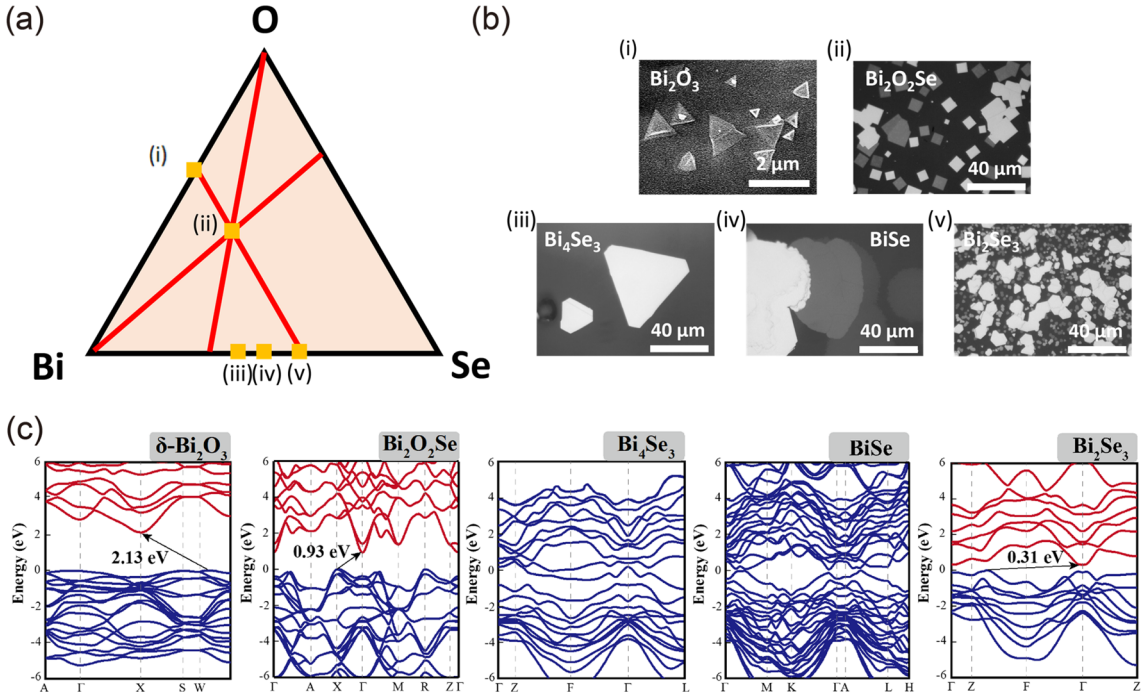

Figure 3. Phase controlled growth of various bismuth compounds. (a) Schematic of Bi−O−Se ternary phase diagram. (b) SEM (i) and OM (ii−v) images of bismuth compounds. Panels i−v denote the corresponding phase on panel . (c) Electronic band structures of each grown phase (δ-Bi_2O_3, Bi_2O_2Se, Bi_4Se_3, and BiSe, Bi_2Se_3).

nm) and fast response time (~1 ps).[20−25] However, due to the low vapor pressure of the precursor, powder sublimation generally requires high process temperature and yields to low homogeneity. Therefore, vapor-phase precursors based growth method, which enables precise and low-temperature growth, is required for practical device applications of ternary metal-oxy-chalcogenides. Several vapor-phase processes, such as molecular beam epitaxy,[16] pulsed laser deposition,[26] and so on were developed to improve the controllability, but suitable processes for ternary metal-oxy-chalcogenide are still insufficient.

Here, we report a ternary layered metal-oxy-chalcogenide (*i.e.*, Bi_2O_2Se) growth method using cracking metal−organic chemical vapor deposition (c-MOCVD). Especially, the high-quality single-crystalline epitaxial film was obtained at a low temperature of a minimum 300 °C on $SrTiO_3$ (STO) which has a very small lattice mismatch. Besides, we also confirmed the synthesis of multiple bismuth compounds (Bi_2O_3, Bi_4Se_3, BiSe, and Bi_2Se_3) by controlling the partial pressure of precursors, which provides great advantages in systematical research of ternary systems. Moreover, we demonstrated the FET and photodetector, which showed high electron mobility, photoresponsivity, and fast response time of 127 $cm^2/(V{\cdot}s)$, 45134 A/W, and 4.6 ms. Our works enable systematically exploring ternary metal-oxy-chalcogenides beyond binary layered materials and suggest promising candidates for next-generation (opto-)electronic devices.

RESULTS AND DISCUSSION

Figure 1a shows a schematic image that describes our c-MOCVD process for Bi_2O_2Se growth where triphenyl bismuth ($Bi(Ph)_3$), dimethyl selenide (DMSe), and oxygen are used as precursors. The thermal decomposition temperature of $Bi(Ph)_3$ is around 300 °C,[27] whereas that of DMSe generally used for selenide growth[28−30] is around 600 °C, approaching the thermodynamically unfavored temperature for the Bi_2O_2Se phase.[31] To overcome the gap between the precursor decomposition temperature and the crystal formation temperature, we designed the c-MOCVD to spatially separate the precursor decomposition zone and growth zone, where the decomposed precursors are delivered to the growth zone through the carrier gas. This process enables formation of the stable Bi_2O_2Se phase as well as achieving the low growth temperature, which is around 300−400 °C (see Experimental Methods for details). Panels b−d of Figure 1 and Figure 2 deal with representative results of Bi_2O_2Se nanoplate grown on fluorophlogopite mica and single-crystalline epitaxial thin film grown on STO, respectively. Figure 1b displays a representative optical image of the resulting c-MOCVD-grown Bi_2O_2Se flake and its corresponding atomic force microscopy (AFM) image. Supporting Information Figure S1 presents further images of the grown samples. The MOCVD-grown Bi_2O_2Se has a domain size of several tens of micrometers, and its thickness ranges from 2.4 to 40 nm depending on growth conditions such as temperature and time (see Figure S1). The thickness distribution of Bi_2O_2Se on mica is presented in Figure S2. To confirm the crystal structure of Bi_2O_2Se nanoplates grown on mica substrate, cross-sectional scanning transmission electron microscopy (STEM) was performed (Figure 1c). Because the intensity is approximately proportional to $Z^{\sim 2}$ (Z is an atomic number) in the high-angle annular dark-field (HAADF) STEM images,[32] bright bismuth atoms and relatively dark selenium atoms were identified, which well matched with the structure of Bi_2O_2Se viewed as the [100] zone axis. Also, oxygen atoms present at Bi_2O_2 layers were directly visualized through annular bright-field (ABF) STEM. In addition, atomic-scale elemental analysis was conducted *via* energy-dispersive X-ray spectroscopy (EDS) mapping (Figure 1d), which confirmed that Bi_2O_2 layers and Se layers alternate along the *c*-axis without other impurities. Below, using the MOCVD growth method, which has

https://doi.org/10.1021/acsnano.1c00811
ACS Nano 2021, 15, 8715−8723

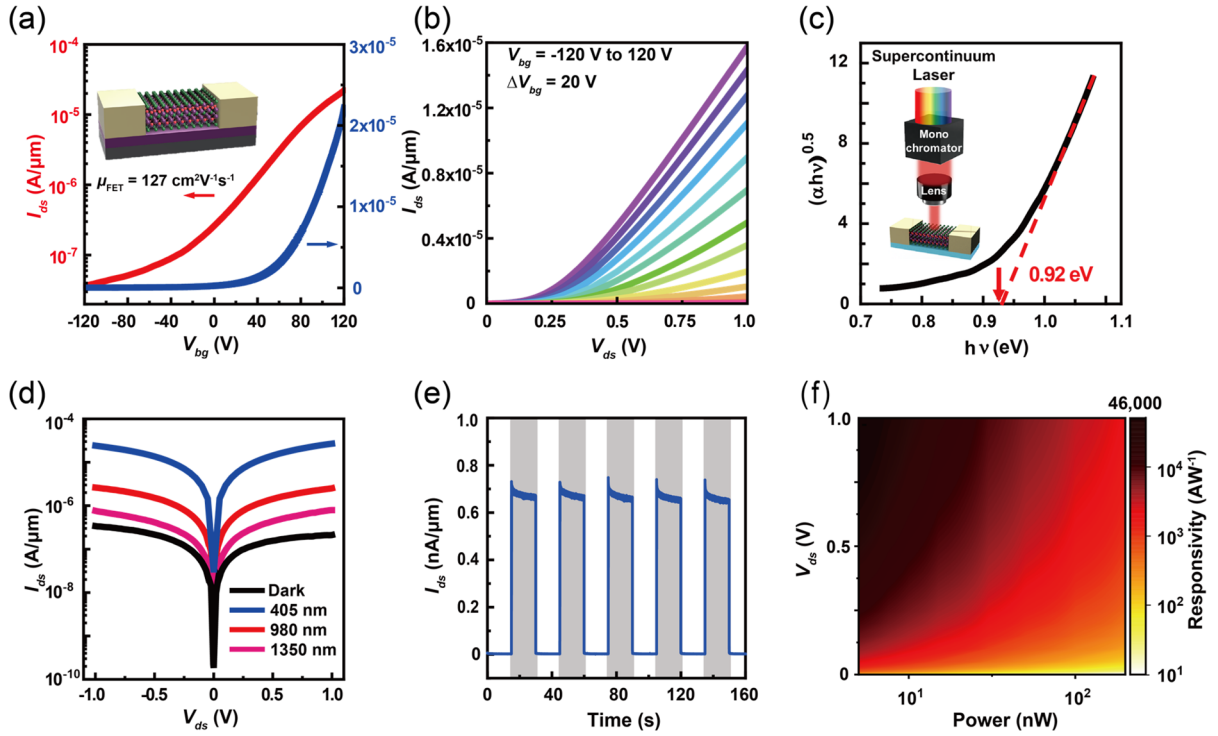

Figure 4. Electrical and optoelectronic properties of Bi_2O_2Se FET and photodetector. (a) Transfer characteristics and (b) output characteristics of multilayer Bi_2O_2Se FET with different back-gate voltage applied. The inset shows a schematic image of back-gate Bi_2O_2Se FET. (c) Plot of $(\alpha h\nu)^{0.5}$ *vs* $h\nu$ for determination of optical band gap of Bi_2O_2Se. The inset shows a schematic image of Bi_2O_2Se photodetector under monochromatic laser. (d) log-scale *I*–*V* characteristics of Bi_2O_2Se photodetector under dark and 405 nm, 980 nm, and 1350 nm laser irradiation. (e) Photoresponse of the device using 405 nm laser with incident power of 100 nW. (f) Dependence of responsivity with different incident power and V_{ds} bias with 405 nm laser irradiation.

conventionally excellent film quality and high controllability, we will discuss the growth of high-quality single-crystalline Bi_2O_2Se (Figure 2) and phase control under the Bi–O–Se ternary system (Figure 3). Later on, excellent electrical and optoelectronic properties of these MOCVD-grown Bi_2O_2Se are also discussed (Figure 4).

Figure 2 shows the low-temperature (~300 °C) single-crystalline epitaxial growth of Bi_2O_2Se on the STO (001) substrate using our c-MOCVD. Panels a–c of Figure 2 are representative AFM images of Bi_2O_2Se film on STO substrate at different growth times. Initially, Bi_2O_2Se was grown in the Volmer–Weber mode along the terrace of STO formed by annealing (Figure 2a,b), and when growth continued, islands coalesced to form a continuous film (Figure 2c). The thickness of islands, before the coalescence, was about 45 nm, and route mean square roughness of thin film formed after coalescence was 3.63 nm. In contrast to the annealed substrate, on the STO substrate without step surface, square-shaped Bi_2O_2Se flakes were nucleated, and a thicker film was formed (Figure S3). This phenomenon can be ascribed to the high nucleation rate at the step edge.[33,34] Panels d and e of Figure 2 show the results of the HAADF-STEM image and its fast Fourier transform (FFT) pattern of Bi_2O_2Se film on the STO substrate. As shown in Figure 2d, it was confirmed that the atoms of STO and Bi_2O_2Se are well arranged in a row, respectively. In addition, the FFT pattern shows the epitaxial relationship between Bi_2O_2Se film and STO substrate with Bi_2O_2Se (002)//STO (001) and Bi_2O_2Se [100]//STO [100], where the yellow and orange circles indicate the patterns of Bi_2O_2Se and STO, respectively (Figure 2e). To examine the overall structural properties of Bi_2O_2Se thin film, high-resolution X-ray diffraction (HRXRD) measurement was performed. Figure 2f shows the 2θ–ω scan of Bi_2O_2Se film grown on the STO substrate. Only the family peaks of the (001)-plane were observed, which means that the out-of-plane texture is perfectly *c*-axis-oriented. The estimated lattice parameter of *c*-axis using the diffracted 2θ value is 12.15 Å, which is consistent with the theoretical value.[12] Furthermore, to determine the quality of the out-of-plane texture of films, rocking curves were obtained for the (004)-plane (Figure 2g). The full width at half-maximum (fwhm) of Bi_2O_2Se showed 0.08°, which indicates high crystallinity compared to other conventional MOCVD epitaxial films.[35,36] In-plane orientation of Bi_2O_2Se thin film was confirmed using ϕ scan method for the off-axis (013)-plane in Figure 2h. The diffracted peaks of the Bi_2O_2Se (013)-planes were found to match those of the STO substrate for (011)-planes by spacing 90° intervals, representing the epitaxial relationship between Bi_2O_2Se film and STO substrate with the 4-fold symmetry. Considering in-plane lattice mismatch between Bi_2O_2Se and STO substrate, XRD reciprocal space mapping (RSM) adjacent to the (011) diffraction from the STO substrate was analyzed to study the in-plane strain of the epitaxial Bi_2O_2Se film grown on STO substrate (Figure 2i). One can notice that the Q_y peak position of the (013) diffraction of Bi_2O_2Se was aligned vertically from the peak of (011) of the STO substrate along the Q_y axis, which indicates that the lattice constant of Bi_2O_2Se film along the in-plane axis is the same as that of the STO substrate, representing a fully strained nature over the whole Bi_2O_2Se thin film. Detailed information on reciprocal space mapping is explained in the Supporting Information Figure S4. Through the epitaxial growth and the corresponding structural analysis

https://doi.org/10.1021/acsnano.1c00811
ACS Nano 2021, 15, 8715–8723

results in Figure 2, we confirm that our MOCVD growth process is suitable for high-quality Bi_2O_2Se growth at the low temperature (~300 °C).

The capability of the precise and individual flow control in our MOCVD process enables us to achieve the various phases of bismuth-oxy-selenide, as shown in Figure 3. Figure 3a shows a ternary phase diagram of the Bi−O−Se system, and the compositions of the phases (Bi_2O_3, Bi_2O_2Se, Bi_4Se_3, BiSe, Bi_2Se_3) that we observed are marked on it. Figure 3b shows the representative scanning electron microscopy (SEM) and optical microscopy (OM) images of each phase. Among the growth parameters in our MOCVD, we figured out that the oxygen concentration majorly affects the growth behaviors. Figure S5a shows the coverage and phases of resulting materials depending on the oxygen flow rate, and the corresponding $2\theta-\omega$ XRD data are exhibited in Figure S5b−f. First, the Bi_4Se_3 phase is formed (Figure S5d) at zero flow of O_2. Second, the Bi_2O_2Se phase is generated (Figure S5c) at 0.3 sccm of O_2 flow. When the O_2 flow was between the optimum condition of Bi_4Se_3 and Bi_2O_2Se phases, the coverage of grown films drastically decreased (Figure S5a). In this O_2 flow range, we deduced that Bi_4Se_3 is oxidized, but there is insufficient oxygen to form Bi_2O_2Se so that the nucleation and growth are suppressed.[37] Third, Bi_2O_2Se was fully oxidized to Bi_2O_3 over 0.4 sccm. Moreover, we investigated the phase changes depending on the concentration of selenium precursor $(CH_3)_2Se$), observing phase transition from Bi_4Se_3 to BiSe and Bi_2Se_3 (Figure S5e,f) under excess Se condition in our MOCVD.[38] In addition, the electronic structures of each grown phase were estimated by computational simulation based on density functional theory (DFT) to indirectly understand the electrical and optical properties of each phase (Figure 3c). The band gap of each phase was predicted by generalized gradient approximation within Perdew, Burke, and Ernzerhof (GGA-PBE) method, and the underestimated band gap was corrected by Heyd−Scuseria−Ernzerhof hybrid functionals (HSE06) with the inclusion of spin−orbit coupling (GGA-PBE-SOC and HSE-SOC) (see Experimental Methods for details). Note that Bi_2Se_3 was exceptionally calculated only at the GGA-PBE-SOC level due to the abnormally underestimated band gap prediction at the HSE-SOC.[39] The resulting band gaps cover from metallic to wide-band-gap semiconducting where the calculated band gaps of each phase are as follows; BiSe, semimetallic; Bi_4Se_3, semimetallic; Bi_2Se_3, 0.31 eV; Bi_2O_2Se, 0.93 eV; Bi_2O_3, 2.13 eV. The precise phase control demonstration in Figure 3 manifests another advantage of our MOCVD process in the investigation of the Bi−O−Se material system.

To confirm the quality of c-MOCVD-grown Bi_2O_2Se as an electronic material, we demonstrated FET and photodetector as shown in Figure 4. The grown Bi_2O_2Se was transferred onto SiO_2 (300 nm)/Si substrate, and we fabricated back-gate FET devices (see Experimental Methods for details). Panels a and b of Figure 4 show the transfer curve and output curve of a representative Bi_2O_2Se FET device, where drain current (I_{ds}) changes as a function of the back-gate voltage (V_{bg}) and drain current changes as a function of source-drain voltage (V_{ds}), respectively. The inset in Figure 4a depicts a schematic image of the Bi_2O_2Se FET structure. The mobility of the Bi_2O_2Se FET at room temperature shows an excellent value of 127 $cm^2/(V\cdot s)$, where the field-effect mobility is calculated using the dI_{ds}/dV_{bg} slope of the linear section of the transfer curve. The device transconductance G_m (dI_{ds}/dV_{bg}) shows a high value of 6.3 μS (0.44 $\mu S/\mu m$), despite the fact that we used thick SiO_2 as a gate dielectric whose capacitance is relatively low. We observed that Bi_2O_2Se FET exhibits a typical n-type characteristic, which shows an exponential increase in I_{ds} with the increase in V_{bg}, and the on/off current ratio is 10^3 showing an on current of 10^{-5} A/μm and an off current of 10^{-8} A/μm. Additional FET devices were also fabricated and measured, and the results are exhibited in Figures S6 and S7. Also, to confirm the air stability of Bi_2O_2Se, we measured the optical reflectance image and electrical characteristics of Bi_2O_2Se nanoplates before and after nearly a year passed as shown in Figure S8. The optical contrast of Bi_2O_2Se nanoplates barely changed in the reflectance image (Figure S8a). The on/off ratio, FET mobility, and on current changed less than 7% (Figure S8b).

To investigate the optoelectronic characteristic of Bi_2O_2Se, the Bi_2O_2Se photodetector was directly fabricated on a mica substrate as a metal−semiconductor−metal (MSM) type device without passivation. Figure 4c shows the spectral response of Bi_2O_2Se photodetector, and it can be derived from the spectral responsivity $R = I_{ph}/P$ ($I_{ph} = I_{illuminated} - I_{dark}$) shown in Figure S9a, where I_{ph} is the spectral photocurrent and P is the optical power. The inset depicts the schematic image of Bi_2O_2Se photodetector under the monochromatic laser. By extrapolating linear region of $(\alpha h\nu)^{0.5}$ *vs* $h\nu$ plot, where α is the effective absorption coefficient and $h\nu$ is the energy of the photon, Bi_2O_2Se shows a band gap of 0.92 eV, which is consistent with the DFT calculated value of 0.93 eV in Figure 3c (see Experimental Methods for details). Figure 4d shows the current change of the photodetector before and after the laser irradiation. When irradiating a laser with wavelengths of 405 nm (5 nW), 980 nm (1 uW), and 1350 nm (1 uW), it is confirmed that the current significantly increases compared with the dark current. This result shows that Bi_2O_2Se based photodetector has a broad spectral response range that covers ultraviolet, visible, and even near-infrared. Figure 4e shows the time-dependent photocurrent measurement of the Bi_2O_2Se photodetector without passivation under air while the laser (405 nm, 100 nW) is switched on and off repeatedly, and the shaded area indicates when the laser irradiation is on. During the time-dependent photocurrent measurement, an optical chopper is used for blocking the irradiation of the laser. Bi_2O_2Se photodetector shows highly stable on/off switching with a constant photocurrent which exhibits excellent reproducibility of the device. Rise time (τ_{rise}) is the time taken for the photocurrent to reach 10 to 90% of I_{max}, the maximum drain current, and the decay time (τ_{decay}) is the time interval to reach 90 to 10% of I_{max}. The nonpassivated Bi_2O_2Se photodetector under air presents the values of τ_{rise} = 4.6 ms and τ_{decay} = 5.3 ms with highly stable on/off switching level, shown in Figure S9b, which exhibits superior response time properties compared with other binary layered materials.[40−42] Figure 4f is the color chart drawn to show the photoresponsivity of Bi_2O_2Se with various bias and power values under 405 nm laser irradiation using the following equation: $R = I_{ph}/P_{in}$. Bi_2O_2Se shows the highest responsivity when a high bias is applied and low-power laser is irradiated, which means that carrier transit time is effectively controlled by the bias voltage, suggesting the high quality of the synthesized crystal. Moreover, Bi_2O_2Se showed a high responsivity of 45134 A/W when a laser with a power of 5 nW was irradiated. In addition to responsivity and response time, detectivity, the main figure of merits of a photodetector, is evaluated. Figure S9c shows the

https://doi.org/10.1021/acsnano.1c00811
ACS Nano 2021, 15, 8715−8723

specific detectivity as a function of laser power, and the maximum specific detectivity of Bi_2O_2Se is 3.3×10^{13} jones, which is equal to or higher than detectivity of the commercial Si photodetector.[43] Additionally, thickness-dependent optoelectronic characteristics of Bi_2O_2Se photodetector are shown in Figure S10. The Bi_2O_2Se photodetector showed increases in dark current, photocurrent, responsivity, and detectivity as a function of thickness. Throughout the results from Figure 4, the high performances of Bi_2O_2Se based FET and photodetector are successfully demonstrated.

CONCLUSIONS

In summary, we developed a gas-phase growth of high-quality Bi_2O_2Se *via* c-MOCVD at a low temperature (~300 °C). Using our c-MOCVD advantage, we successfully demonstrated the single-crystalline epitaxial growth of Bi_2O_2Se on STO, precise phase control, and the high-performance FETs and photodetectors. We believe that the c-MOCVD process can provide more opportunities for Bi_2O_2Se and related materials research in the near future. For example, the MOCVD growth process is applicable to the other metal-oxy-chalcogenide growth, such as Bi_2O_2S, Bi_2O_2Te, and so on. Until now, Bi_2O_2S and Bi_2O_2Te have been rarely investigated due to their narrow range of chemically stable composition.[44] It is possible to grow Bi_2O_2S and Bi_2O_2Te by utilizing precise partial pressure control of MOCVD. In addition, the growth of lateral or vertical heterostructure of metal-oxy-chalcogenide can be achieved using the function of the sequential flow of different precursors in MOCVD.[30,45] Furthermore, our MOCVD process can be adapted to the CMOS process due to its low growth temperature, and the gas-phase process can also be applied to batch fabrication.[46]

EXPERIMENTAL METHODS

Growth of MOCVD Bi_2O_2Se. Bi_2O_2Se was grown using a homemade MOCVD setup equipped with a 2-in.-diameter horizontal quartz tube. A mica substrate (freshly cleaved from a fluorophlogopite mica) was used for Bi_2O_2Se nanoplate growth. A perovskite oxide STO (001) substrate, which has a 0.6% lattice mismatch with Bi_2O_2Se, was used for epitaxial film growth. Before growth on the STO substrate, the chemical treatment was performed to generate a Ti-terminated step surface through the following method. The STO substrate was treated by ultrasonication in acetone, IPA, and DI water for 5 min each, maintaining a temperature over 60 °C. Afterward, the cleaned STO was soaked in buffered oxide etchant at 10% for 5 min, followed by thermal annealing at 1000 °C for 10 h in the air to form the step surface. Triphenyl bismuth ($Bi(C_6H_5)_3$) and dimethyl selenide ($(CH_3)_2Se$) were used as metal (Bi) and chalcogenide (Se) precursors, respectively. Oxygen gas—O_2—was used as the oxidation source. Each precursor was precisely regulated by a mass flow controller (MFC). Because Bi precursor has relatively low vapor pressure, $Bi(C_6H_5)_3$ was directly injected into the chamber by flowing Ar gas controlled by MFC from the front end of the canister. $(CH_3)_2Se$ was kept in bubblers at a constant pressure of 800 Torr and carried by Ar carrier gas. The $Bi(C_6H_5)_3$ canister was heated to 130 °C, and the gas line, from canister to chamber inlet, was heated to 140 °C in order to prevent the line from sticking. Our optimized flow rates of precursors are 200 sccm for $Bi(C_6H_5)_3$, 0.4 sccm for $(CH_3)_2Se$, 0.3 sccm for O_2, and 200 sccm for Ar. The total pressure is 7.2 Torr in-process. The two-heating zone was necessary to simultaneously guarantee a sufficient amount of precursor pyrolysis and nucleation. The front zone, which controls the amount of precursor pyrolysis, is named cracking zone, and the back zone, where Bi_2O_2Se is grown, is named growth zone. The optimum conditions were different depending on the substrate. The temperature of the cracking zone/growth zone was 450 °C/430 °C for mica substrate, and 430 °C/300 °C for STO substrate.

Characterization. An image of atomically thin bismuth-oxychalcogenides was obtained by field-emission scanning electron microscopy (FE-SEM, Hitachi S-4800), optical microscopy (Olympus), and AFM (NNOVA-LABRAM HR800). The phase and crystallinity were confirmed by X-ray diffraction (XRD, Rigaku, Smartlab) with Cu Kα radiation using high-resolution mode. In-plane orientation and RSM were measured by HRXRD (Panalytical X'pert MRD) with a four-bounce Ge (022) monochromator. The cross-sectional samples for STEM imaging were prepared by focused ion beam (FIB, FEI Helios NanoLab 450). Then, cross-sectional STEM images were obtained using a FEI Titan[3] G2 60-300 operating at 200 kV. Energy-dispersive X-ray (EDS) spectroscopic imaging was performed by a SuperX EDX spectrometer.

Electronic Structure Calculations. The first-principles calculations based on density functional theory were performed using the Vienna *ab initio* simulation package (VASP).[47−49] Projector augmented-wave (PAW) pseudopotentials with a kinetic energy cutoff of 450 eV for the plane-wave basis set were used.[50] The generalized gradient approximation within Perdew, Burke, and Ernzerhof scheme with inclusion of spin−orbit coupling was utilized to describe the exchange−correlation potential,[51] and the van der Waals (vdW) correction was included by using the DFT-D2 method.[52] For structure optimizations, $17 \times 17 \times 11$ γ-centered k-point mesh was taken. All atomic positions and lattice constants were optimized using the conjugate gradient method by setting the convergence criteria on the total energy and force to 10^{-6} eV and 10^{-2} eV/Å, respectively. The electronic band structures were also calculated by using Heyd−Scuseria−Ernzerhof hybrid functionals to correct the underestimated band gap values.[53]

Fabrication of Transistor and Photodetector. To fabricate the bottom gate Bi_2O_2Se FET, Bi_2O_2Se was transferred to SiO_2 (300 nm)/Si (n++) substrate using PMMA based wet transfer method. After transfer, conventional photolithography was conducted on the source, drain pattern, and Ti and Au metal electrodes were sequentially deposited at thicknesses of 10 and 30 nm, respectively, by an e-beam evaporator. Ti was selected as a contact electrode since it has a low workfunction of 4.3 eV and matches well with the workfunction of n-type semiconductor. The lift-off process was done by dipping the sample in photoresist remover (AZ Kwik strip remover) annealed at 100 °C for 1 h.

In the case of photodetector fabrication, conventional photolithography, e-beam evaporation, and lift-off process were identically done to Bi_2O_2Se grown on a mica substrate. Metal−semiconductor−metal-type Bi_2O_2Se photodetector without passivation was fabricated.

PMMA Based Wet Transfer Method. PMMA was spin-coated on the mica substrate, which is covered with Bi_2O_2Se flakes, at the rate of 1500 rpm for a minute. After the spin coating is done, the substrate is placed on a hot plate with the temperature of 150 °C for 90 s. Then the mica was dipped in a diluted HF solution with a concentration of 2% for a couple of hours. Before dipping, the edge of the mica was removed by a razor blade to enhance penetration of the HF solution into the interface of PMMA and mica. A couple of hours later, the PMMA that holds Bi_2O_2Se flakes was separated from the mica. PMMA with Bi_2O_2Se flakes was then rinsed with deionized water and scooped with 300 nm SiO_2/Si substrate. Finally, the substrate was dipped in acetone for 24 h to remove PMMA.

Electrical and Optoelectronic Parameter Calculation. Field-effect mobility was extracted from the following equation: $\mu_{FET} = [L/(WC_{ox}V_{ds})]\,[dI_{ds}/dV_{bg}]$. L is the channel length, W is the channel width, C_{ox} is gate oxide capacitance per unit area, V_{ds} is the voltage between source and drain, and V_{bg} is the gate voltage. The mobility of Bi_2O_2Se FET was calculated using the following device parameters: $L = 3.5$ μm, $W = 14.4$ μm, $C_{ox} = 1.15 \times 10^{-4}$ F m^{-2} ($C_{ox} = \varepsilon_0\varepsilon_r/t_{ox}$, $\varepsilon_r = 3.9$, $t_{ox} = 300$ nm), and $V_{ds} = 1$ V.

The spectral response was induced by converting R to effective absorption coefficient α by the relation $\alpha = -1/t\,\ln(1 - R h\nu/e\eta)$, where t is the thickness of the channel layer, $h\nu$ is the energy of the photon, and η is the internal quantum efficiency. Through the

https://doi.org/10.1021/acsnano.1c00811
ACS Nano 2021, 15, 8715−8723

equation above $(\alpha h\nu)^m = A(h\nu - E_g)$ is induced, where m is the exponent determined by the type of transition and E_g is the band gap of the semiconductor, which can be expressed by α and $h\nu$ values. Since Bi_2O_2Se shows indirect band gap transition, the band gap is obtained by extrapolating the linear region of the $(\alpha h\nu)^{0.5}$ *vs* $h\nu$ plot.

Electrical and Optoelectronic Characterization. The electrical characterization of Bi_2O_2Se FET was performed under ambient condition using a semiconductor parameter analyzer system (Keithley instrument—4200 SCS). The spectral photocurrent was measured using a supercontinuum laser with a monochromator (NKT photonics—SuperK extreme). To keep the intensity of the supercontinuum laser constant, the precisely adjusted power table was used during the operation of the monochromator. Time-dependent photoresponse and repetitive photoresponse with and without laser irradiation were measured by low noise current preamplifier (SRS-SR570) and data acquisition system (National Instrument—NI 6343 X Series Data Acquisition). Irradiation of laser was blocked using an optical chopper system (Scitec instrument—300 CD).

ASSOCIATED CONTENT

Supporting Information

The Supporting Information is available free of charge at https://pubs.acs.org/doi/10.1021/acsnano.1c00811.

(Figures S1−S3, S8a) OM, AFM, and SEM images; (Figure S4) reciprocal space mapping; (Figure S5) flow rate phase change dependence; (Figures S6, S7, and S8b) top gate FETs electrical and transfer characteristics; (Figures S9 and S10) optoelectronic characteristics (PDF)

AUTHOR INFORMATION

Corresponding Authors

Kibum Kang − *Department of Materials Science and Engineering, Korea Advanced Institute of Science and Technology (KAIST), Daejeon 34141, Republic of Korea; Advanced Nanosensor Research Center, KI Nanocentury, Korea Advanced Institute of Science and Technology (KAIST), Daejeon 34141, Republic of Korea;* orcid.org/0000-0003-1674-1826; Email: kibumkang@kaist.ac.kr

Hu Young Jeong − *UNIST Central Research Facilities (UCRF) and Department of Materials Science and Engineering, Ulsan National Institute of Science and Technology (UNIST), Ulsan 44919, Republic of Korea;* orcid.org/0000-0002-5550-5298; Email: hulex@unist.ac.kr

Sung-Yool Choi − *School of Electrical Engineering, Graphene/2D Materials Research Center, Center for Advanced Materials Discovery towards 3D Display, Korea Advanced Institute of Science and Technology (KAIST), Daejeon 34141, Republic of Korea;* orcid.org/0000-0002-0960-7146; Email: sungyool.choi@kaist.ac.kr

Seungwoo Song − *Operando Methodology and Measurement Team, Korea Research Institute of Standards & Science (KRISS), Daejeon 34113, Republic of Korea;* orcid.org/0000-0002-8524-3444; Email: swsong@kriss.re.kr

Authors

Minsoo Kang − *Department of Materials Science and Engineering, Korea Advanced Institute of Science and Technology (KAIST), Daejeon 34141, Republic of Korea;* orcid.org/0000-0001-8419-4997

Hyun-Jun Chai − *Department of Materials Science and Engineering, Korea Advanced Institute of Science and Technology (KAIST), Daejeon 34141, Republic of Korea*

Han Beom Jeong − *Department of Materials Science and Engineering, Korea Advanced Institute of Science and Technology (KAIST), Daejeon 34141, Republic of Korea*

Cheolmin Park − *School of Electrical Engineering, Graphene/2D Materials Research Center, Center for Advanced Materials Discovery towards 3D Display, Korea Advanced Institute of Science and Technology (KAIST), Daejeon 34141, Republic of Korea*

In-young Jung − *Department of Physics, Hanyang University, Seoul 04763, Republic of Korea; Operando Methodology and Measurement Team, Korea Research Institute of Standards & Science (KRISS), Daejeon 34113, Republic of Korea*

Eunpyo Park − *Center for Neuromorphic Engineering, Korea Institute of Science and Technology (KIST), Seoul 02792, Republic of Korea*

Mert Miraç Çiçek − *Department of Engineering Physics, Faculty of Engineering, Ankara University, Ankara 06100, Turkey; UNAM—National Nanotechnology Research Center and Institute of Materials Science and Nanotechnology, Bilkent University, Ankara 06800, Turkey*

Injun Lee − *Wearable Platform Materials Technology Center (WMC), Korea Advanced Institute of Science and Technology (KAIST), Daejeon 34141, Republic of Korea*

Byeong-Soo Bae − *Wearable Platform Materials Technology Center (WMC), Korea Advanced Institute of Science and Technology (KAIST), Daejeon 34141, Republic of Korea;* orcid.org/0000-0001-9424-1830

Engin Durgun − *UNAM—National Nanotechnology Research Center and Institute of Materials Science and Nanotechnology, Bilkent University, Ankara 06800, Turkey;* orcid.org/0000-0002-0639-5862

Joon Young Kwak − *Center for Neuromorphic Engineering, Korea Institute of Science and Technology (KIST), Seoul 02792, Republic of Korea;* orcid.org/0000-0002-7799-8812

Complete contact information is available at: https://pubs.acs.org/10.1021/acsnano.1c00811

Author Contributions

⊡M.K. and H.-J.C. contributed equally to this work.

Funding

This research was supported by the National R&D Program through the National Research Foundation of Korea (NRF) funded by the Ministry of Science and ICT (Grant Nos. 2018R1C1B6008176, 2020M3F3A2A01081899, 2020M3D1A1110659, 2020M3F3A2A01082618, 2016M3D1A1900035, and 2020R1C1C1014257), the Korea Institute of Science and Technology (KIST) Institutional Program (Grant No. 2 V07080-19-P148), the Wearable Platform Materials Technology Center (WMC) funded by the NRF by the Korean Government (MSIT) (Grant No. 2016R1A5A1009926), and the POSCO Science fellowship.

Notes

The authors declare no competing financial interest.

ACKNOWLEDGMENTS

We thank J. Y. Kim for help in preparing the manuscript.

REFERENCES

(1) Duan, X.; Wang, C.; Pan, A.; Yu, R.; Duan, X. Two-Dimensional Transition Metal Dichalcogenides as Atomically Thin Semiconduc-

tors: Opportunities and Challenges. *Chem. Soc. Rev.* **2015**, *44* (24), 8859−8876.
(2) Chhowalla, M.; Shin, H. S.; Eda, G.; Li, L. J.; Loh, K. P.; Zhang, H. The Chemistry of Two-Dimensional Layered Transition Metal Dichalcogenide Nanosheets. *Nat. Chem.* **2013**, *5* (4), 263−275.
(3) Song, C.; Noh, G.; Kim, T. S.; Kang, M.; Song, H.; Ham, A.; Jo, M.; Cho, S.; Chai, H.; Cho, S. R.; Cho, K.; Park, J.; Song, S.; Song, I.; Bang, S.; Kwak, J. Y.; Kang, K. Growth and Interlayer Engineering of 2D Layered Semiconductors for Future Electronics. *ACS Nano* **2020**, *14* (12), 16266−16300.
(4) Geum, D.-M.; Kim, S.; Khym, J.; Lim, J.; Kim, S.; Ahn, S.-Y.; Kim, T. S.; Kang, K.; Kim, S. Arrayed MoS_2−$In_{0.53}Ga_{0.47}As$ van der Waals Heterostructure for High-Speed and Broadband Detection from Visible to Shortwave-Infrared Light. *Small* **2021**, *17*, 2007357.
(5) Kim, Y.; Cruz, S. S.; Lee, K.; Alawode, B. O.; Choi, C.; Song, Y.; Johnson, J. M.; Heidelberger, C.; Kong, W.; Choi, S.; Qiao, K.; Almansouri, I.; Fitzgerald, E. A.; Kong, J.; Kolpak, A. M.; Hwang, J.; Kim, J. Remote Epitaxy through Graphene Enables Two-Dimensional Material-Based Layer Transfer. *Nature* **2017**, *544* (7650), 340−343.
(6) Kang, K.; Lee, K. H.; Han, Y.; Gao, H.; Xie, S.; Muller, D. A.; Park, J. Layer-by-Layer Assembly of Two-Dimensional Materials into Wafer-Scale Heterostructures. *Nature* **2017**, *550* (7675), 229−233.
(7) Koma, A. Van der Waals Epitaxy-A New Epitaxial Growth Method for a Highly Lattice-Mismatched System. *Thin Solid Films* **1992**, *216* (1), 72−76.
(8) Geim, A. K.; Grigorieva, I. V. Van der Waals Heterostructures. *Nature* **2013**, *499* (7459), 419−425.
(9) Zhong, Y.; Cheng, B.; Park, C.; Ray, A.; Brown, S.; Mujid, F.; Lee, J.-U.; Zhou, H.; Suh, J.; Lee, K.-H.; Mannix, A. J.; Kang, K.; Sibener, S. J.; Muller, D. A.; Park, J. Wafer-Scale Synthesis of Monolayer Two-Dimensional Porphyrin Polymers for Hybrid Superlattices. *Science (Washington, DC, U. S.)* **2019**, *366* (6471), 1379−1384.
(10) Desai, S. B.; Madhvapathy, S. R.; Sachid, A. B.; Llinas, J. P.; Wang, Q.; Ahn, G. H.; Pitner, G.; Kim, M. J.; Bokor, J.; Hu, C.; Wong, H. S. P.; Javey, A. MoS_2 Transistors with 1-Nanometer Gate Lengths. *Science (Washington, DC, U. S.)* **2016**, *354* (6308), 99−102.
(11) Liu, Y.; Duan, X.; Huang, Y.; Duan, X. Two-Dimensional Transistors beyond Graphene and TMDCs. *Chem. Soc. Rev.* **2018**, *47* (16), 6388−6409.
(12) Wu, J.; Yuan, H.; Meng, M.; Chen, C.; Sun, Y.; Chen, Z.; Dang, W.; Tan, C.; Liu, Y.; Yin, J.; Zhou, Y.; Huang, S.; Xu, H. Q.; Cui, Y.; Hwang, H. Y.; Liu, Z.; Chen, Y.; Yan, B.; Peng, H. High Electron Mobility and Quantum Oscillations in Non-Encapsulated Ultrathin Semiconducting Bi_2O_2Se. *Nat. Nanotechnol.* **2017**, *12* (6), 530−534.
(13) Wu, J.; Tan, C.; Tan, Z.; Liu, Y.; Yin, J.; Dang, W.; Wang, M.; Peng, H. Controlled Synthesis of High-Mobility Atomically Thin Bismuth Oxyselenide Crystals. *Nano Lett.* **2017**, *17* (5), 3021−3026.
(14) Tu, T.; Zhang, Y.; Li, T.; Yu, J.; Liu, L.; Wu, J.; Tan, C.; Tang, J.; Liang, Y.; Zhang, C.; Dai, Y.; Han, Y.; Lai, K.; Peng, H. Uniform High-k Amorphous Native Oxide Synthesized by Oxygen Plasma for Top-Gated Transistors. *Nano Lett.* **2020**, *20* (10), 7469−7475.
(15) Li, T.; Tu, T.; Sun, Y.; Fu, H.; Yu, J.; Xing, L.; Wang, Z.; Wang, H.; Jia, R.; Wu, J.; Tan, C.; Liang, Y.; Zhang, Y.; Zhang, C.; Dai, Y.; Qiu, C.; Li, M.; Huang, R.; Jiao, L.; Lai, K.; Yan, B.; Gao, P.; Peng, H. A Native Oxide High-κ Gate Dielectric for Two-Dimensional Electronics. *Nat. Electron.* **2020**, *3*, 473−478.
(16) Liang, Y.; Chen, Y.; Sun, Y.; Xu, S.; Wu, J.; Tan, C.; Xu, X.; Yuan, H.; Yang, L.; Chen, Y.; Gao, P.; Guo, J.; Peng, H. Molecular Beam Epitaxy and Electronic Structure of Atomically Thin Oxyselenide Films. *Adv. Mater.* **2019**, *31* (39), 1901964.
(17) Cheng, T.; Tan, C.; Zhang, S.; Tu, T.; Peng, H.; Liu, Z. Raman Spectra and Strain Effects in Bismuth Oxychalcogenides. *J. Phys. Chem. C* **2018**, *122* (34), 19970−19980.
(18) Wu, M.; Zeng, X. C. Bismuth Oxychalcogenides: A New Class of Ferroelectric/Ferroelastic Materials with Ultra High Mobility. *Nano Lett.* **2017**, *17* (10), 6309−6314.
(19) Wu, J.; Yuan, H.; Meng, M.; Chen, C.; Sun, Y.; Chen, Z.; Dang, W.; Tan, C.; Liu, Y.; Yin, J.; Zhou, Y.; Huang, S.; Xu, H. Q.; Cui, Y.; Hwang, H. Y.; Liu, Z.; Chen, Y.; Yan, B.; Peng, H. High Electron Mobility and Quantum Oscillations in Non-Encapsulated Ultrathin Semiconducting Bi_2O_2Se. *Nat. Nanotechnol.* **2017**, *12* (6), 530−534.
(20) Tian, X.; Luo, H.; Wei, R.; Zhu, C.; Guo, Q.; Yang, D.; Wang, F.; Li, J.; Qiu, J. An Ultrabroadband Mid-Infrared Pulsed Optical Switch Employing Solution-Processed Bismuth Oxyselenide. *Adv. Mater.* **2018**, *30* (31), 1801021.
(21) Yang, H.; Chen, W.; Zheng, X.; Yang, D.; Hu, Y.; Zhang, X.; Ye, X.; Zhang, Y.; Jiang, T.; Peng, G.; Zhang, X.; Zhang, R.; Deng, C.; Qin, S. Near-Infrared Photoelectric Properties of Multilayer Bi_2O_2Se Nanofilms. *Nanoscale Res. Lett.* **2019**, *14* (1), 371.
(22) Luo, P.; Zhuge, F.; Wang, F.; Lian, L.; Liu, K.; Zhang, J.; Zhai, T. PbSe Quantum Dots Sensitized High-Mobility Bi_2O_2Se Nanosheets for High-Performance and Broadband Photodetection beyond 2 Mm. *ACS Nano* **2019**, *13* (8), 9028−9037.
(23) Tong, T.; Chen, Y.; Qin, S.; Li, W.; Zhang, J.; Zhu, C.; Zhang, C.; Yuan, X.; Chen, X.; Nie, Z.; Wang, X.; Hu, W.; Wang, F.; Liu, W.; Wang, P.; Wang, X.; Zhang, R.; Xu, Y. Sensitive and Ultrabroadband Phototransistor Based on Two-Dimensional Bi_2O_2Se Nanosheets. *Adv. Funct. Mater.* **2019**, *29* (50), 1905806.
(24) Yin, J.; Tan, Z.; Hong, H.; Wu, J.; Yuan, H.; Liu, Y.; Chen, C.; Tan, C.; Yao, F.; Li, T.; Chen, Y.; Liu, Z.; Liu, K.; Peng, H. Ultrafast and Highly Sensitive Infrared Photodetectors Based on Two-Dimensional Oxyselenide Crystals. *Nat. Commun.* **2018**, *9* (1), 3311.
(25) Fu, Q.; Zhu, C.; Zhao, X.; Wang, X.; Chaturvedi, A.; Zhu, C.; Wang, X.; Zeng, Q.; Zhou, J.; Liu, F.; Tay, B. K.; Zhang, H.; Pennycook, S. J.; Liu, Z. Ultrasensitive 2D Bi_2O_2Se Phototransistors on Silicon Substrates. *Adv. Mater.* **2019**, *31* (1), 1804945.
(26) Song, Y.; Li, Z.; Li, H.; Tang, S.; Mu, G.; Xu, L.; Peng, W.; Shen, D.; Chen, Y.; Xie, X.; Jiang, M. Epitaxial Growth and Characterization of High Quality Bi_2O_2Se Thin Films on $SrTiO_3$ Substrates by Pulsed Laser Deposition. *Nanotechnology* **2020**, *31* (16), 165704.
(27) Kang, S.-W.; Rhee, S.-W. Evaluation of Precursors for DLI MOCVD of Ferroelectric BLT. *J. Electrochem. Soc.* **2003**, *150* (9), C573.
(28) Eichfeld, S. M.; Hossain, L.; Lin, Y. C.; Piasecki, A. F.; Kupp, B.; Birdwell, A. G.; Burke, R. A.; Lu, N.; Peng, X.; Li, J.; Azcatl, A.; McDonnell, S.; Wallace, R. M.; Kim, M. J.; Mayer, T. S.; Redwing, J. M.; Robinson, J. A. Highly Scalable, Atomically Thin WSe_2 Grown *via* Metal-Organic Chemical Vapor Deposition. *ACS Nano* **2015**, *9* (2), 2080−2087.
(29) Lee, C.-S.; Jin, G.; Seo, S.-Y.; Kim, J.; Han, C.; Park, M. Y.; Ahn, H.; Lee, S.-H.; Cha, S.; Jo, M.-H. Programmed Band Gap Modulation within van der Waals Semiconductor Monolayers by Metalorganic Vapor-Phase Epitaxy. *Chem. Mater.* **2020**, *32* (12), 5084−5090.
(30) Xie, S.; Tu, L.; Han, Y.; Huang, L.; Kang, K.; Lao, K. U.; Poddar, P.; Park, C.; Muller, D. A.; DiStasio, R. A.; Park, J. Coherent, Atomically Thin Transition-Metal Dichalcogenide Superlattices with Engineered Strain. *Science (Washington, DC, U. S.)* **2018**, *359* (6380), 1131−1136.
(31) Khan, U.; Luo, Y.; Tang, L.; Teng, C.; Liu, J.; Liu, B.; Cheng, H. M. Controlled Vapor−Solid Deposition of Millimeter-Size Single Crystal 2D Bi_2O_2Se for High-Performance Phototransistors. *Adv. Funct. Mater.* **2019**, *29* (14), 1807979.
(32) Jesson, D. E.; Pennycook, S. J. Incoherent Imaging of Crystals Using Thermally Scattered Electrons. *Proc. R. Soc. London. Ser. A Math. Phys. Eng. Sci.* **1995**, *449* (1936), 273−293.
(33) Sánchez, F.; Ocal, C.; Fontcuberta, J. Tailored Surfaces of Perovskite Oxide Substrates for Conducted Growth of Thin Films. *Chem. Soc. Rev.* **2014**, *43* (7), 2272−2285.
(34) Chen, L.; Liu, B.; Ge, M.; Ma, Y.; Abbas, A. N.; Zhou, C. Step-Edge-Guided Nucleation and Growth of Aligned WSe_2 on Sapphire *via* a Layer-over-Layer Growth Mode. *ACS Nano* **2015**, *9* (8), 8368−8375.
(35) Nakamura, S.; Mukai, T.; Senoh, M. *In Situ* Monitoring and Hall Measurements of GaN Grown with GaN Buffer Layers. *J. Appl. Phys.* **1992**, *71* (11), 5543−5549.

https://doi.org/10.1021/acsnano.1c00811
ACS Nano 2021, 15, 8715−8723

(36) Kobayashi, K.; Matsubara, T.; Matsushima, S.; Shirakata, S.; Isomura, S.; Okada, G. Preparation of C-Axis Oriented ZnO Films by Low-Pressure Organometallic Chemical Vapor Deposition. *Thin Solid Films* **1995**, *266* (2), 106−109.
(37) Kong, D.; Cha, J. J.; Lai, K.; Peng, H.; Analytis, J. G.; Meister, S.; Chen, Y.; Zhang, H. J.; Fisher, I. R.; Shen, Z. X.; Cui, Y. Rapid Surface Oxidation as a Source of Surface Degradation Factor for Bi_2Se_3. *ACS Nano* **2011**, *5* (6), 4698−4703.
(38) Springholz, G.; Wimmer, S.; Groiss, H.; Albu, M.; Hofer, F.; Caha, O.; Kriegner, D.; Stangl, J.; Bauer, G.; Holý, V. Structural Disorder of Natural Bi_mSe_n Superlattices Grown by Molecular Beam Epitaxy. *Phys. Rev. Mater.* **2018**, *2* (5), 054202.
(39) Park, S.; Ryu, B. Hybrid-Density Functional Theory Study on the Band Structures of Tetradymite-Bi_2Te_3, Sb_2Te_3, Bi_2Se_3, and Sb_2Se_3 Thermoelectric Materials. *J. Korean Phys. Soc.* **2016**, *69* (11), 1683−1687.
(40) Zhang, W.; Huang, J.-K.; Chen, C.-H.; Chang, Y.-H.; Cheng, Y.-J.; Li, L.-J. High-Gain Phototransistors Based on a CVD MoS_2 Monolayer. *Adv. Mater.* **2013**, *25* (25), 3456−3461.
(41) Lopez-Sanchez, O.; Lembke, D.; Kayci, M.; Radenovic, A.; Kis, A. Ultrasensitive Photodetectors Based on Monolayer MoS_2. *Nat. Nanotechnol.* **2013**, *8* (7), 497−501.
(42) Choi, M. S.; Qu, D.; Lee, D.; Liu, X.; Watanabe, K.; Taniguchi, T.; Yoo, W. J. Lateral MoS_2 *p*−*n* Junction Formed by Chemical Doping for Use in High-Performance Optoelectronics. *ACS Nano* **2014**, *8* (9), 9332−9340.
(43) Manders, J. R.; Lai, T.-H.; An, Y.; Xu, W.; Lee, J.; Kim, D. Y.; Bosman, G.; So, F. Low-Noise Multispectral Photodetectors Made from All Solution-Processed Inorganic Semiconductors. *Adv. Funct. Mater.* **2014**, *24* (45), 7205−7210.
(44) Sun, Y.; Zhang, J.; Ye, S.; Song, J.; Qu, J. Progress Report on Property, Preparation, and Application of Bi_2O_2Se. *Adv. Funct. Mater.* **2020**, *30* (49), 2004480.
(45) Gong, Y.; Lin, J.; Wang, X.; Shi, G.; Lei, S.; Lin, Z.; Zou, X.; Ye, G.; Vajtai, R.; Yakobson, B. I.; Terrones, H.; Terrones, M.; Tay, B. K.; Lou, J.; Pantelides, S. T.; Liu, Z.; Zhou, W.; Ajayan, P. M. Vertical and In-Plane Heterostructures from WS_2/MoS_2 Monolayers. *Nat. Mater.* **2014**, *13* (12), 1135−1142.
(46) Kang, K.; Xie, S.; Huang, L.; Han, Y.; Huang, P. Y.; Mak, K. F.; Kim, C.-J.; Muller, D.; Park, J. High-Mobility Three-Atom-Thick Semiconducting Films with Wafer-Scale Homogeneity. *Nature* **2015**, *520* (7549), 656−660.
(47) Kresse, G.; Furthmüller, J. Efficient Iterative Schemes for *ab Initio* Total-Energy Calculations Using a Plane-Wave Basis Set. *Phys. Rev. B: Condens. Matter Mater. Phys.* **1996**, *54* (16), 11169−11186.
(48) Hohenberg, P.; Kohn, W. Inhomogeneous Electron Gas. *Phys. Rev.* **1964**, *136* (3B), B864−B871.
(49) Kohn, W.; Sham, L. J. Self-Consistent Equations Including Exchange and Correlation Effects. *Phys. Rev.* **1965**, *140* (4A), A1133−A1138.
(50) Blöchl, P. E. Projector Augmented-Wave Method. *Phys. Rev. B: Condens. Matter Mater. Phys.* **1994**, *50* (24), 17953−17979.
(51) Perdew, J. P.; Burke, K.; Ernzerhof, M. Generalized Gradient Approximation Made Simple. *Phys. Rev. Lett.* **1996**, *77* (18), 3865−3868.
(52) Grimme, S. Semiempirical GGA-Type Density Functional Constructed with a Long-Range Dispersion Correction. *J. Comput. Chem.* **2006**, *27* (15), 1787−1799.
(53) Heyd, J.; Scuseria, G. E.; Ernzerhof, M. Hybrid Functionals Based on a Screened Coulomb Potential. *J. Chem. Phys.* **2003**, *118* (18), 8207−8215.

https://doi.org/10.1021/acsnano.1c00811
ACS Nano 2021, 15, 8715−8723